

Article

Geology and Genesis of Xianglushan Fe-Cu Orefield in Sichuan (SW China): Evidence from C-O-S-Pb Isotopes

Tianguo Wang ¹, Chunkit Lai ^{2,3,*}  and Huan Li ¹ 

¹ Key Laboratory of Metallogenic Prediction of Nonferrous Metals and Geological Environment Monitoring, Ministry of Education, School of Geosciences and Info-Physics, Central South University, Changsha 410083, China; wangtianguo@csu.edu.cn (T.W.); lihuan@csu.edu.cn (H.L.)

² Faculty of Science, Universiti Brunei Darussalam, Gadong BE1410, Brunei

³ Centre of Excellence in Ore Deposits (CODES), University of Tasmania, Tasmania 7001, Australia

* Correspondence: chunkitl@utas.edu.au; Tel.: +673-879-1488

Received: 16 March 2019; Accepted: 28 May 2019; Published: 1 June 2019



Abstract: The Proterozoic Xianglushan Fe-Cu orefield (western Sichuan) is located in the Huili–Dongchuan ore belt on the southwestern margin of the Yangtze Block in SW China. The orefield has experienced complex magmatotectonic activities, and hosts a wide variety of Fe oxide-(Cu-Au) deposits. At Xianglushan, the orebodies are made of stratabound magnetite–hematite orebodies superimposed by vein-type chalcopyrite mineralization. The stratabound Fe orebodies are hosted mainly in the Proterozoic volcanic-sedimentary rocks of the lower Yinmin Formation, whilst the Cu vein or stockwork ores were mainly emplaced into the upper part of the footwall volcanic rocks and the lower part of the Fe orebodies. We divided the alteration/mineralization and their fluid inclusions (FIs) into the (I) sodic-calcic alteration, (II) potassic-silicic-sericite alteration and Fe-(Cu) mineralization, and (III) carbonate alteration and Cu mineralization stages. Stage II FIs are mainly two-phase (vapor-liquid), and are featured by medium temperature (348 to 379 °C) and high salinity (21.8 to 22.9 wt % NaCl eqv). Their generally negative calcite $\delta^{13}\text{C}$ (−4.1‰ to −3.1‰) and $\delta^{18}\text{O}_{\text{H}_2\text{O}}$ (12.2‰ to 15.3‰) values reveal that the Stage II ore fluids have had a seawater-magmatic fluid mixed source. Late Stage II pyrite has $\delta^{34}\text{S}$ (−3.3‰ to 13.7‰), $^{206}\text{Pb}/^{204}\text{Pb}$ (17.663 to 18.982), $^{207}\text{Pb}/^{204}\text{Pb}$ (15.498 to 15.824) and $^{208}\text{Pb}/^{204}\text{Pb}$ (37.784 to 38.985), suggesting that the ore-forming materials were derived from dominantly upper crustal source. Stage III FIs are also mainly two-phase (vapor-liquid), and are featured by lower temperature (206 to 267 °C) and salinity (19.0 to 22.5 wt % NaCl eqv) than their Stage II counterparts. The Stage III ore fluids were also likely derived from a meteoric–magmatic mixed source with greater magmatic influence, as indicated by the generally negative calcite $\delta^{13}\text{C}$ (−6.9‰ to −4.6‰) and $\delta^{18}\text{O}_{\text{H}_2\text{O}}$ (6.3‰ to 9.2‰) values. Similar to the late Stage II pyrite, the Stage III chalcopyrite $\delta^{34}\text{S}$ (−4.6‰ to 5.2‰) and Pb isotopes ($^{206}\text{Pb}/^{204}\text{Pb}$ = 18.198 to 18.987; $^{207}\text{Pb}/^{204}\text{Pb}$ = 15.534 to 15.876; and $^{208}\text{Pb}/^{204}\text{Pb}$ = 37.685 to 39.476) also suggest a crustal ore-forming material source. Therefore, we suggest that the Fe-(Cu) and Cu mineralization at Xianglushan had similar ore fluid and material sources, although the magmatic influence increased in the later stage. This resembles many Fe-(Cu) deposits in the Huili–Dongchuan ore belt. We conclude that the Xianglushan Fe-Cu deposits are both similar to and different from typical iron-oxide copper gold (IOCG) deposits in terms of alteration styles and hydrothermal mineral assemblages, and are thus best classified as IOCG-like deposits hosted in submarine volcanic-sedimentary rocks. Considering the Mesoproterozoic regional tectonics in the southwestern Yangtze Block, we propose that the Xianglushan ore formation occurred in an intra-/back-arc inversion setting, possibly related to the closure of the Anning ocean basin.

Keywords: IOCG-like deposit; Sichuan (SW China); submarine volcanics; calcite C-O isotopes; sulfide Pb-S isotopes; fluid inclusions; Proterozoic; Yangtze Block

1. Introduction

The Huili–Dongchuan ore belt in western Sichuan is located on the southwestern margin of the Yangtze craton, and has experienced various phases of tectonomagmatic activities [1–7]. The ore belt contains a number of large-medium Fe-Cu deposits, such as Lala, Xikuangshan, Luoxue, Yinmin, and Tangdan, and is an important Fe-Cu mineral province in China [8]. The ore belt is geographically divided by the Jinshajiang River into an eastern and a western part. Previous mineral exploration and research have been mostly dedicated to the eastern part (i.e., the Dongchuan section), whereas the western part (i.e., Huili section) was poorly explored or understood. The recent discovery of the Xianglushan orefield represents a major exploration breakthrough in the Huili section, where previously only the Lala deposit and a few prospects were found. For a long time, the deposit type of the Xianglushan deposits has been loosely constrained as volcanic-sedimentary types, but recently there are also suggestions that some of these deposits (e.g., Lala) are of IOCG-type/-like [9–11].

This paper represents the first international publication on Fe-Cu deposits from the Xianglushan orefield; we present new fluid inclusions and C-O-S-Pb isotopes data for the ore-related calcite from the Xianglushan Fe-Cu orefield. Integrated with ore deposit geological and alteration/mineralization features, we discuss the deposit type, and ore fluid and material sources at Xianglushan.

2. Regional Geological Background

The Huili–Dongchuan ore belt (125 × 80 km) is an aulacogen located in the northern part of the Kangdian rift zone in the western Yangtze Craton (Figure 1a). The ore belt is bounded by the Xiaojiang fault to the east, the Mopanshan fault to the west, the Tianbaoshan–Qiaojia fault to the south, and the Dingtaicang–Jiulong fault to the north. The ore belt is cut into the Lala–Tianbaoshan, Tongan–Lunanshan, and Xiaojie–Dongchuan ore sections by the N-S-trending Yimen–Luchang and Puduhe faults (Figure 1b).

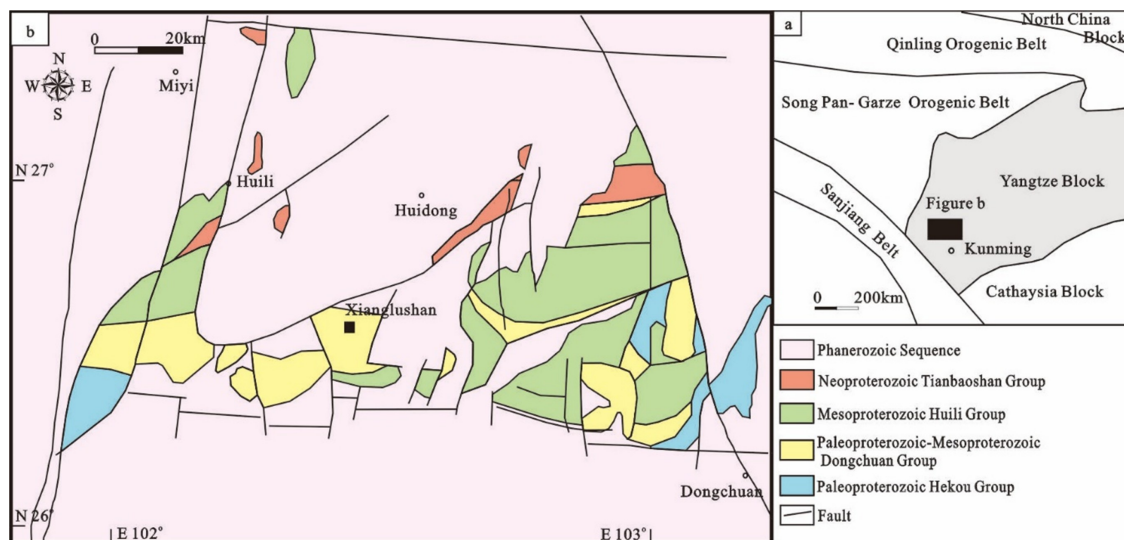


Figure 1. (a) Tectonic map of the Yangtze Block; (b) Simplified geologic map of the Huili–Dongchuan area (modified from Liu et al. [12]).

Proterozoic metamorphic rocks constitute the main exposed stratigraphy in the area [12,13], and are the main Fe-Cu ore host (Figure 2). Multiple phases of well-developed deformation (folding and faulting) are reported in the ore district, which controlled the distribution of magmatism and mineralization. Folding in the district affected both the Proterozoic basement rocks and the overlying upper Cretaceous sequence. Faults are complex and with multiphase reactivation, leading to difficulties in determining their ages. General direction of faulting progressed from EW → NW → NE → NW trending, and the fault reactivation caused mutual crosscutting of these faults (Figures 1 and 2).

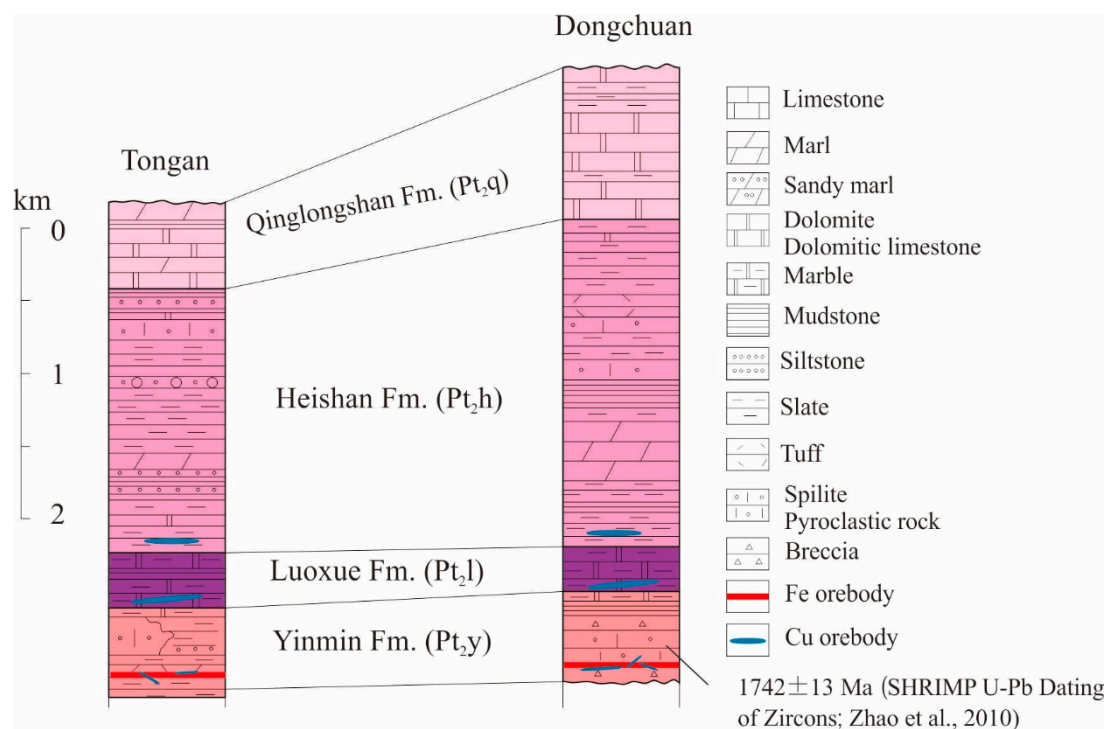


Figure 2. Stratigraphic comparison of Tongan–Dongchuan area.

In the Huili–Dongchuan region, magmatic rocks are widespread and exposed mainly along the EW-trending fold axis and N-S trending faults. Previous geochronological studies in the region suggested six magmatic phases: (I) early Paleoproterozoic, (II) late Paleoproterozoic (Yinmin Period), (III) early Mesoproterozoic (Heishan Period), (IV) Neoproterozoic (Jinningian–Chengjiang Period), (V) late Permian (late Hercynian Period), and (VI) Cretaceous. Phase I magmatism was mainly represented by the Hekou Group (Lala area) and Kunyang Group (Dongchuan area), which consist mainly of bimodal magmatic rocks, e.g., spilite, tuffs (zircon U-Pb age: 2.3 Ga), and sub-volcanic rocks [14,15]. Phase II magmatism is represented mainly by intraplate volcanic rocks of the Yinmin Formation (Dongchuan Group) in the Dongchuan–Tongan area. The Yinmin Formation (zircon U-Pb age: 1.8 to 1.6 Ga) contains mainly Fe-Cu-ore hosting (e.g., Xikuangshan deposit) spilite and minor keratophyre [16–19]. Phase III (zircon U-Pb age: 1.5 Ga) magmatic rocks are mainly distributed in the Dongchuan–Tongan area, and include mainly intraplate tuffs and spilite with mafic intrusions. The volcanic rocks are the ore host for the regional Ti-V magnetite mineralization (e.g., Zhuqing deposit) [5]. Neoproterozoic granites are mainly distributed along the Jinshajiang, Chenhe, and Tongan areas, among which the Changtang batholith (size: 8 km²) is closely related to W-Sn mineralization. In the Lala-Dongchuan area, Neoproterozoic gabbroic/doleritic dykes (Pb model ages: 984 to 747 Ma) intruded into the Proterozoic sequences and are in close spatial relationship with many Fe-Cu deposits (e.g., Lala and Dongchuan) [20]. Late Permian mafic stocks and dykes are widespread, and comprise mainly basalts, olivine-phyric sub-volcanics, dolerite, and gabbro. Cretaceous magmatic rocks are mainly distributed in the Dongchuan–Boka area, and comprise mainly aplite dykes that intruded into the Kunyang and Dongchuan Groups (zircon U-Pb age: 128.2 ± 1.5 Ma) [21].

3. Deposit Geology

3.1. Stratigraphy and Structures

Exposed sequences in the Xianglushan Orefield include the Yinmin Formation (Dongchuan Group), Luoxue Formation, Heishan Formation, Qinglongshan Formation, Tangtang Formation (Huili Group), and Quaternary sediments (Figure 3). The Yinmin Formation (exposed mainly at

Pingzi, Xianglushan, and Yaopengzi) can be divided into an upper and a lower member. The upper Yinmin Formation comprises purplish argillaceous dolomite and tuffaceous shale interbeds (60 to 80 m thick). The lower Yinmin Formation (main Fe-Cu ore-hosting sequences) comprises a suite of mafic volcanic/volcaniclastic rocks, including spilite, volcanic breccias, tuffs, and tuffaceous shale. The breccias (>600 m thick) contain complex clast compositions, including both volcanic and gabbroic rocks. The Heishan Formation in the orefield is distributed to the west of Yaopengzi fault, and includes carbonaceous/sandy shale and siltstone interbeds (over 100 m thick). The Yinmin Formation spilite is the ore host at the Yaopengzi ore-section, and is mainly layered and massive or amygdaloidal. The spilite contains mainly plagioclase (30–40%) and altered pyroxene (20–30%), and minor secondary epidote (<10%), chlorite (<10%), Fe-Ti oxides (<10%), sericite (<5%), and calcite (<5%) (Figure 4A,B).

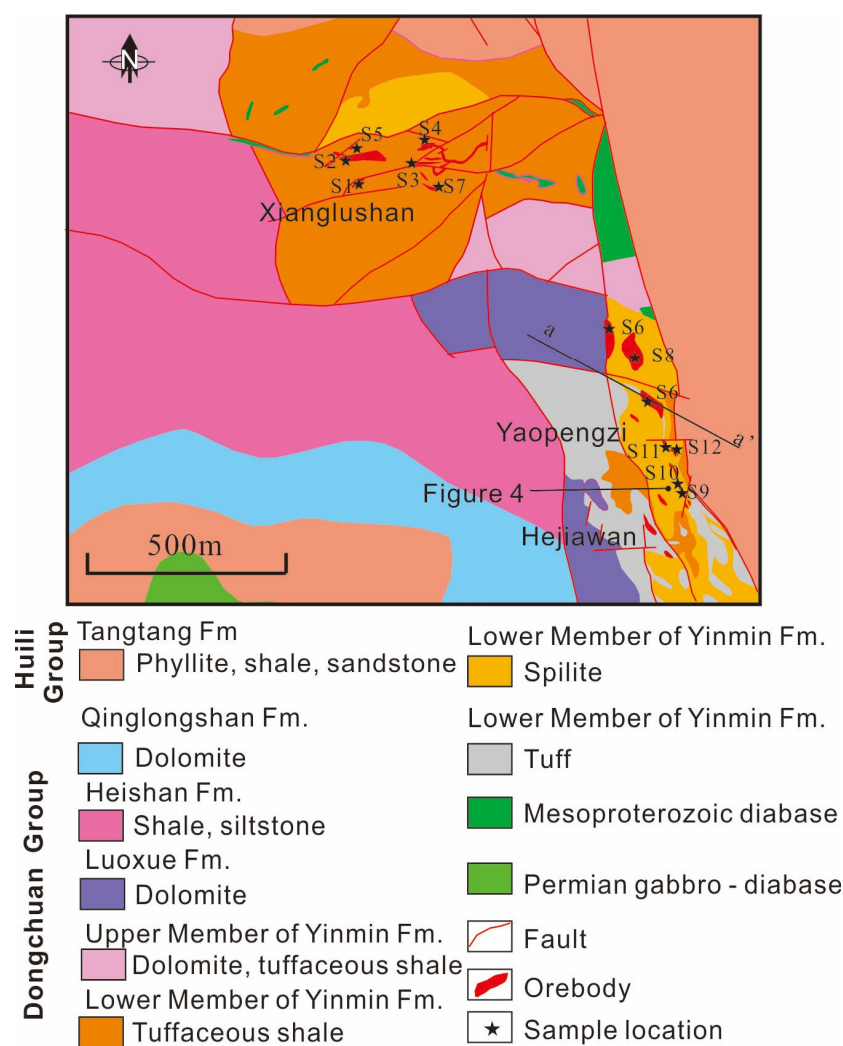


Figure 3. Geologic map of the Xianglushan area.

The carbonaceous shale contains large amount of pyrite. Some of these shales are Cu-bearing, notably those in the Dongchuan–Taoyuan area. The Luoxue Formation (exposed mainly in the western Xianglushan) is composed mainly of (cherty)-dolomite. The Qinglongshan Formation (Dongchuan Group; exposed mainly in the southwestern Xianglushan) contains mainly medium-thick-bedded (>50 m) calcic-dolomite. The Tangtang Formation (equivalent to the Shuangshuijing Formation in the Huili area and Dayingpan Formation in the Dongchuan area) is widely exposed in northwestern and eastern Xianglushan. Major rock types include dark greyish phyllite and interbeds of purplish-red sandy shale, sandstone, and conglomerate. Hematite mineralization is found at the bottom of the

formation. Intrusive rocks are widely found in outcrops and underground mine tunnels, and include mainly gabbroic and doleritic dykes.



Figure 4. Field and thin-section petrographic photos of the Yinmin Formation spilite, showing (A) massive structure; (B) amygdaloidal texture; (C) spilite texture (plane polar); and (D) spilite texture (crossed polar). Abbreviations: Pl = Plagioclase; Mag = Magnetite; Chl = Chlorite.

Influenced by the regional deformation, structures (fault/fracture and fold) in the Xianglushan orefield are well developed and highly complex. The main fold in the orefield is the Xianglushan anticline, which is distributed to the west of Yaopengzi fault. The anticline (2 km long and 0.8 km wide) is E-W-trending and N-plunging. The anticlinal core is composed of the tuffaceous sandy shale of the lower Yinmin Formation, whilst the limbs are composed of the purplish shale of the upper Yinmin Formation and the Luoxue Formation dolomite. The anticlinal core is crosscut by several EW-trending faults (F_8 , F_{11} , and F_{13}), and the major Xianglushan orebodies are hosted in the anticlinal axis. The anticlinal core is crosscut by several EW-trending faults (F_8 , F_{11} , and F_{13}), and the major Xianglushan orebodies are hosted in the anticlinal axis.

Around 20 faults are documented in the orefield. The EW- and NS-trending ones are ore-controlling structures (orebodies are either hosted in these faults or are parallel with them), whereas the NE- and NW-trending ones are commonly smaller, post-mineralization, and occasionally ore-destructive. EW-trending faults are mainly distributed in western Xianglushan, notably the Pingzi-Xianglushan, Shuangfenbao, Lengchang-Yaopengzi, and the Zhangmuliangzi-Majialaolin faults. These faults are mostly compressive shears that were first active before the mineralization. The NS-trending faults are mainly distributed in southwestern Xianglushan (e.g., Yaopengzi ore section), and are also mostly compressive shears. Major ones include the Yaopengzi, Kesongliangzi–Xianglushan, and the Hejiawan–Shuangfenbao faults.

3.2. Alteration and Mineralization Features

The Xianglushan Fe-Cu orebodies are mainly stratiform and vein-type in the volcanic-sedimentary sequences of the lower Yinmin Formation. Iron mineralization is mainly hosted in the lower Yinmin Formation, which comprises dolomite, tuff, tuffaceous/Fe-rich slate, and spilite (Figures 5 and 6A). Orebodies in the Xianglushan ore-section (northern Xianglushan orefield) are EW-trending, and the orebody orientation changes progressively to NW-NNW-trending in the Yaopengzi ore-section (southeastern Xianglushan orefield), and then to NS-trending in southern Xianglushan. The Xianglushan ore-section contains mainly tuff-hosted Fe orebodies, whilst the Yaopengzi ore-section contains mainly spilite-hosted Fe-Cu orebodies (Fe-(Cu) ores in the upper part and Cu ores in the lower part). Major ore types include massive/brecciated/banded magnetite and (minor) hematite/maghemite, veined and disseminated chalcopyrite, and supergene limonite and malachite. Metallic minerals include mainly magnetite, chalcopyrite, pyrite, limonite, hematite, and maghemite (Figure 6B–F), whilst non-metallic minerals include mainly quartz, dolomite, micas (incl. biotite and sericite), plagioclase, chlorite, epidote, barite, and clay minerals (e.g., pyrophyllite). Major ore textures include euhedral to anhedral granular and replacement texture, whilst major ore structures include massive, stratiform/stratabound banded, disseminated, veined, stockwork, and brecciated. Wall rocks are commonly intensively and pervasively altered, with major alteration styles including chlorite, epidote, sericite, potassic, hematite, carbonate, and silicic. Among these alteration styles, potassic, silicic, and sericite alterations are closely related to Fe mineralization, whilst carbonatization is closely related to pyrite–chalcopyrite mineralization.

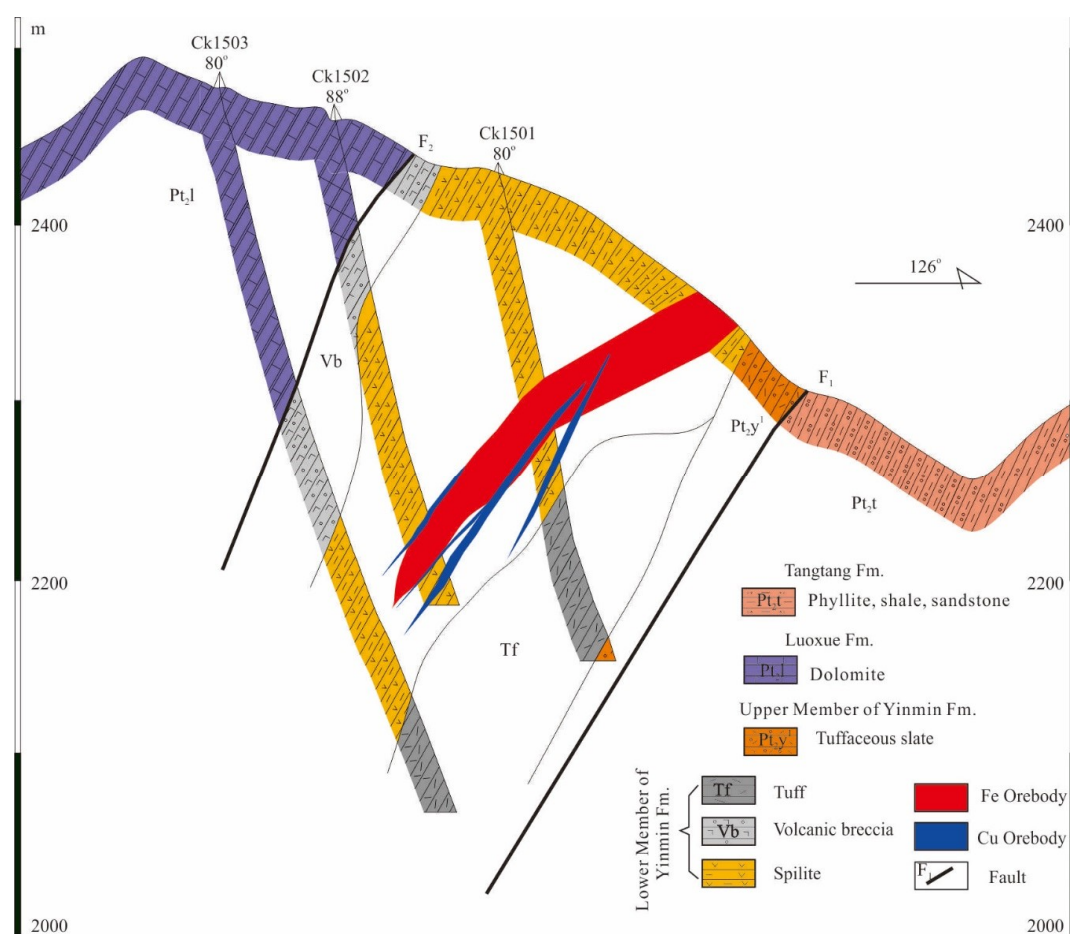


Figure 5. Geological cross-section of the Xianglushan Fe-Cu deposit.

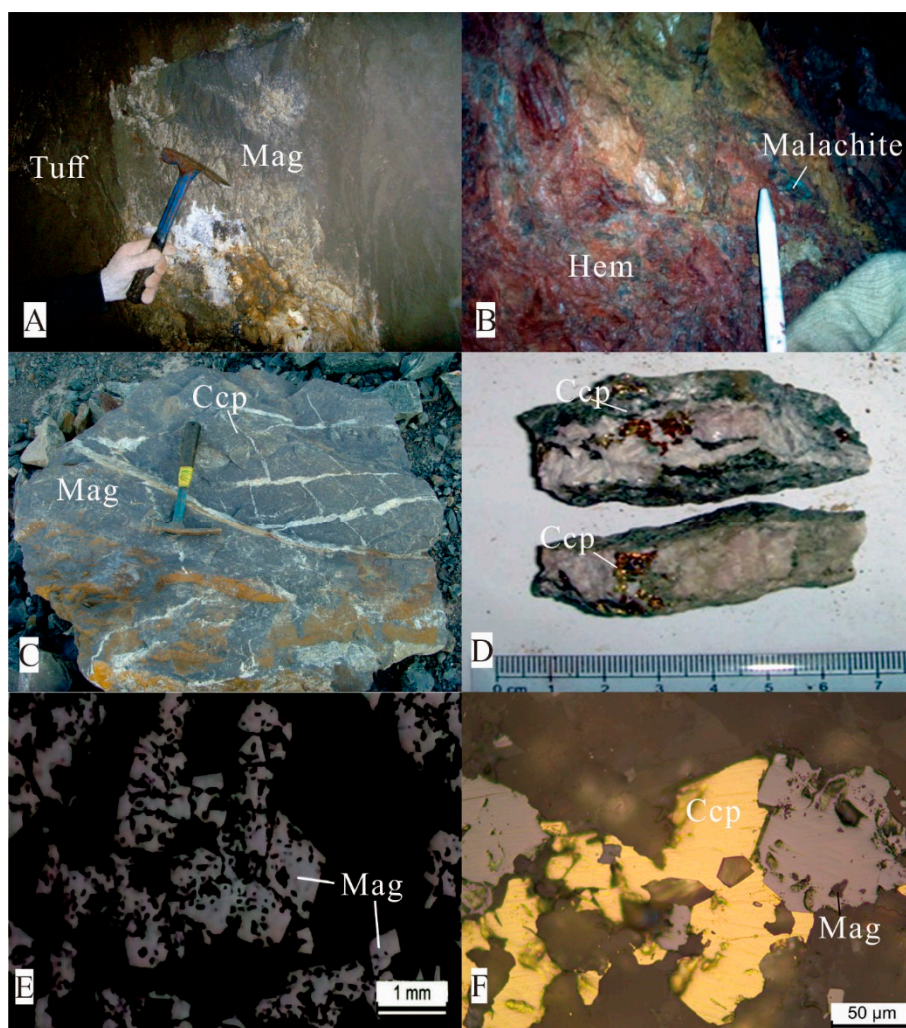


Figure 6. Photos and microphotographs of the Fe-Cu ores at Xianglushan. (A) Massive magnetite ores in contact with tuff (Xianglushan ore section); (B) supergene hematite–malachite ores in spilite (Yaopengzi ore section); (C) disseminated chalcopyrite in massive magnetite ores, crosscut by quartz veins; (D) quartz-chalcopyrite ore veins; (E) massive euhedral–subhedral magnetite; (F) magnetite included in chalcopyrite. Abbreviations: Mag—Magnetite; Hem—Hematite; Ccp—Chalcopyrite.

Based on field geology and ore mineral assemblages, the alteration/mineralization at Xianglushan can be divided into three stages: (I) sodic-calcic alteration, (II) potassic-silicic-sericite alteration and Fe-(Cu) mineralization, and (III) carbonate alteration and Cu mineralization stage (Figure 7). In Stage I, alteration is featured by the formation of albite, epidote, and chlorite in the altered spilite, and the lack of mineralization. Stage II represents the main Fe oxide mineralization (magnetite, maghemite, and hematite), which is associated with potassic (K-feldspar and biotite) and sericite alteration. Minor Cu (disseminated chalcopyrite) mineralization and quartz-sulfide veining occurred in late Stage II and crosscut the early Stage II massive Fe oxide ores. Stage III represents the main Cu mineralization stage, and features the formation of quartz–chalcopyrite veins and carbonatization. Calcite ± quartz veining persisted after Stage III, and shallow orebodies were subjected to later supergene alteration, which formed high-grade limonite–malachite ores.

Mineral \ Stage	Volcanic-sedimentary		Hydrothermal
	I	II	III
Albite	Abundant		
Magnetite		Abundant	
K-feldspar		Abundant	
Chlorite			Trace
Epidote			Trace
Hematite			
Pyrite		Trace	Abundant
Chalcopyrite		Trace	Abundant
Carbonate			Abundant
Quartz	Trace	Abundant	
Sericite	Trace	Abundant	
Barite		Abundant	
Pyrophyllite			Trace

Abundant
 Minor
 Trace

Figure 7. Paragenetic sequence of alteration and mineralization in the Xianglushan Fe-Cu deposits.

4. Methods and Results

4.1. Methods

Four Stage II and two Stage III calcite samples were prepared into double-side polished thin sections. Microthermometric analysis was performed using a Linkam THMSG600 Heating and Freezing Stage, at the Fluid Inclusion Laboratory of the Central South University. The FI salinity was calculated using the FLINCOR procedures with the formula of Brown and Lamb [22].

The FI compositions (including liquid and gas phases) were determined with a Perkin Elmer CLARUS 600 Gas Chromatograph/Mass Spectrometer and a DX-500 Ion Chromatography (IC) System at the Analytical Laboratory Beijing Research Institute of Uranium Geology (ALBRIUG). Four calcite samples (S-01, S-03, S-08, and S-10), with >98% purity, were chosen for the analysis. Concentrations such as K^+ , Na^+ , Ca^{2+} , and Mg^{2+} were measured, and the detailed operational and analytical procedures were similar to those outlined in Wang [23] and Zhu et al. [24].

Carbon-oxygen isotope analyses were conducted at the ALS Laboratory Group (Guangzhou), following similar analytical procedures as described in Guo et al. and Yuan et al. [25,26]. The analyses used the cavity-enhanced absorption spectroscopy with the PDB and SMOW standard. Analysis accuracy was better than $\pm 0.05\%$.

Sulfur and lead isotope analyses of Stage II pyrite (from pyritized Stage II magnetite ore) and Stage III chalcopyrite (from veins crosscutting Stage II ores) were conducted at the same laboratory of ALBRIUG. Sulfur isotope analyses were conducted using a MAT-251 EM mass spectrometer with similar analytical procedures as those outlined in Liu et al. [27]. Pure powdered sulfide samples (200-mesh) were heated in a 1000 °C furnace under vacuum with CuO. After cryogenic separation from other gases, the liberated SO_2 was frozen in a liquid nitrogen trap. All results are reported as per mil (‰) relative to the Canyon Diablo Troilite (CDT), with analysis accuracy better than $\pm 0.2\%$. Sulfide Pb isotope compositions were also analyzed using a MAT-261 and similar method as outlined in Xu et al. and Li et al. [28,29]. Sulfide samples were completely dissolved in ultrapure ($HNO_3 + HCl$) acids at 180 °C. The Pb in the samples was then separated and purified with the two-column AG 1-X8 anion resin technique. Lead isotopic ratios were corrected to the recommended values of Pb NBS-981 standard [30], with analytical reproducibility of 0.1% (2σ) for $^{206}Pb/^{204}Pb$ and $^{207}Pb/^{204}Pb$, and 0.2% (2σ) for $^{208}Pb/^{204}Pb$.

4.2. Fluid Inclusion Types and Features

Stage II calcite occurs mostly as replacement products of magnetite, hematite, and (minor) pyrite and chalcopyrite, whilst Stage III calcite occurs dominantly in stockwork or veinlets. In this study, isolated fluid inclusions and random groups of intragranular calcite crystals were interpreted as primary, whereas those aligned along micro-fractures in trans-granular trails were interpreted as pseudosecondary [31]. Secondary inclusions are too small and unsuitable for analysis. Under the microscope, primary fluid inclusions (size: 2 to 9 μm) are abundant in the calcite samples, and include the following two types: pure liquid (L-type) and vapor-liquid (V-L-type) (Figure 8).

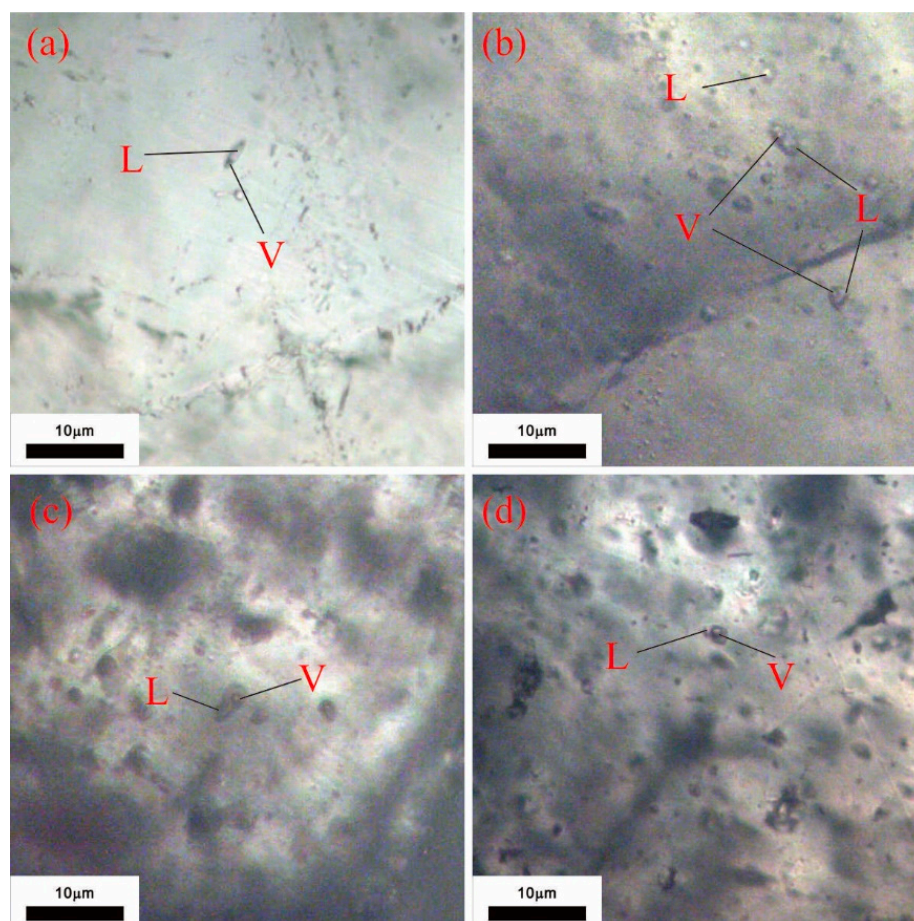


Figure 8. Microphotographs of fluid inclusions (FIs) from the Xianglushan Fe-Cu deposit: L—liquid phase; V—vapor phase. (a) Stage II V-L-type FIs; (b) Stage II L- and V-L-type FIs; (c) Stage III elongated V-L type FIs (bubble: 10 vol.%) (d) Stage III rounded V-L-type FIs (bubble: 30 vol.%).

4.3. Microthermometric Results

The microthermometric results are summarized in Table 1. Stage II fluid inclusions homogenized to liquid at 338 to 379 $^{\circ}\text{C}$ (avg. 361 $^{\circ}\text{C}$). The inclusion ice melting temperatures range from -19.2 to -20.8 $^{\circ}\text{C}$ (avg. -20.2 $^{\circ}\text{C}$). The calculated salinities are of 21.8 to 22.9 (avg. 22.4) wt.% NaCl eqv. Stage III fluid inclusions are homogenized to liquid at 206 to 267 $^{\circ}\text{C}$ (avg. 234 $^{\circ}\text{C}$). The freezing temperatures range from -20.5 to -18.5 $^{\circ}\text{C}$, and the calculated salinities are of 19.0 to 22.5 (avg. 20.4) wt % NaCl eqv.

Table 1. Features of fluid inclusions in ore-related calcite from Xianglushan orefield.

Sample No.	V/L (%)	Size (μm)	Ore Stage
S01	5 to 20	2 to 3	II
S03	5 to 10	2 to 6	
S08	10 to 15	2 to 4	
S09	5 to 20	2 to 4	
S10	10 to 40	2 to 9	III
S11	10 to 30	2 to 6	

Ore Stage	Mineral	Ice Melting Temp ($T_{\text{mice}}/^{\circ}\text{C}$)			Homogenization Temp ($T_{\text{HLV}}/^{\circ}\text{C}$)		Salinity (wt % NaCl eqv.)	
		n	Range	Avg.	Range	Avg.	Range	Avg.
II	Calcite	42	-20.8 to -19.2	-20.2	348 to 379	361	21.8 to 22.9	22.4
III	Calcite	46	-20.5 to -18.5	-19.7	206 to 267	234	19.0 to 22.5	20.4

4.4. Compositions of Fluid Inclusions

Fluid inclusion composition analysis indicates that for the Stage II and III fluid phase components, cations comprise mainly Na^+ and Ca^{2+} , followed by Mg^{2+} and K^+ , whilst anions comprise mainly Cl^- , followed by SO_4^{2-} , and with minor F^- and NO_3^- (Table 2).

Table 2. Compositions of the fluid inclusions in ore-related calcite from Xianglushan orefield.

Sample No.	Mineral	Ore Stage	Liquid Compositions ($\mu\text{g/g}$)							
			F^-	Cl^-	NO_3^-	SO_4^{2-}	K^+	Na^+	Mg^{2+}	Ca^{2+}
S01	Calcite	II	0.713	15.680	0.139	3.640	0.728	7.798	0.561	4.140
S03	Calcite		0.322	31.060	0.209	4.261	1.437	14.120	0.621	4.630
S08	Calcite		0.426	27.910	0.869	5.193	1.160	13.070	1.233	9.250
S10	Calcite	III	1.165	10.350	0.242	9.630	0.452	4.666	1.209	8.610

Sample No.	Mineral	Ore Stage	Gas Compositions ($\mu\text{L/g}$)					
			H_2	N_2	CO	CH_4	CO_2	H_2O
S01	Calcite	II	1.271	2.164	0.168	0.124	10.090	1.180×10^5
S03	Calcite		0.995	1.290	0.162	0.088	10.350	1.616×10^5
S08	Calcite		0.989	0.389	0.200	0.090	11.870	7.517×10^5
S10	Calcite	III	3.460	9.971	0.336	0.446	26.790	3.522×10^5

4.5. Carbon and Oxygen Isotopes

For Stage II calcite, the $\delta^{18}\text{O}_{\text{V-SMOW}}$ and $\delta^{18}\text{C}_{\text{PDB}}$ values are 15.8‰ to 18.6‰ (avg. 17.1‰) and -4.1‰ to -3.1‰ (mean -3.6‰), respectively. For Stage III calcite, the $\delta^{18}\text{O}_{\text{V-SMOW}}$ and $\delta^{18}\text{C}_{\text{PDB}}$ values are 12.4‰ to 15.2‰ (avg. 14.1‰) and -6.9‰ to -4.6‰ (avg. -5.8‰), respectively (Table 3).

Table 3. Carbon-oxygen isotope compositions of calcite from Xianglushan Fe-Cu deposit.

Sample No.	Ore Stage	$\delta^{13}\text{C}_{\text{PDB}}\text{‰}$	$\delta^{18}\text{O}_{\text{V-SMOW}}\text{‰}$	$\delta^{18}\text{O}_{\text{H}_2\text{O}}\text{‰}$	Temperature/ $^{\circ}\text{C}$
S01	II	-3.9	16.2	12.7	361
S03		-3.1	18.6	15.1	
S08		-3.3	17.7	14.2	
S09		-4.1	15.8	12.3	
S10	III	-4.6	12.4	5.0	234
S11		-6.9	15.2	7.8	

Note: Calcite and fluid fractionation is calculated with $1000 \ln \alpha_{\text{Calcite}-\text{H}_2\text{O}} = 2.78 \times 10^6 / T^2 - 3.40$ [32].

4.6. Sulfur and Lead Isotopes

A total of 12 Stage II pyrite and Stage III chalcopyrite samples from various parts of the Xianglushan orefield were analyzed, with the results listed in Table 4.

Table 4. Sulfide S-Pb isotope compositions of the Xianglushan Fe-Cu deposit.

Sample No.	Sample Location	Ore Stage	Ore Type	Mineral	$\delta^{34}\text{S}_{\text{CDT}}/\text{‰}$	$^{206}\text{Pb}/^{204}\text{Pb}$	$^{207}\text{Pb}/^{204}\text{Pb}$	$^{208}\text{Pb}/^{204}\text{Pb}$
S01	Xianglushan	II	Stratiform magnetite	Pyrite	13.7	18.211	15.657	38.280
S02	Xianglushan	II	Stratiform magnetite	Pyrite	6.9	18.869	15.593	38.612
S03	Xianglushan	II	Stratiform magnetite	Pyrite	11.3	17.663	15.498	37.812
S04	Xianglushan	II	Stratiform magnetite	Pyrite	3.2	18.768	15.696	38.972
S06	Yaopengzi	II	Stratiform magnetite	Pyrite	3.3	18.635	15.743	38.985
S08	Yaopengzi	II	Stratiform magnetite	Pyrite	6.7	18.982	15.824	37.784
S09	Yaopengzi	II	Stratiform magnetite	Pyrite	2.8	18.756	15.812	37.952
S12	Yaopengzi	II	Stratiform magnetite	Pyrite	-3.3	18.596	15.736	38.823
S05	Xianglushan	III	Stockwork sulfide	Chalcopyrite	0.9	18.234	15.755	37.658
S07	Xianglushan	III	Stockwork sulfide	Chalcopyrite	5.2	18.676	15.534	38.882
S10	Yaopengzi	III	Stockwork sulfide	Chalcopyrite	-2.6	18.987	15.876	39.476
S11	Yaopengzi	III	Stockwork sulfide	Chalcopyrite	-4.6	18.198	15.581	38.127

Stage II pyrite grains contain $\delta^{34}\text{S}$ of -3.3‰ to $+13.7\text{‰}$ (avg. $+5.6\text{‰}$), and $^{206}\text{Pb}/^{204}\text{Pb}$ (17.663–18.982), $^{207}\text{Pb}/^{204}\text{Pb}$ (15.498–15.824), and $^{208}\text{Pb}/^{204}\text{Pb}$ (37.784–38.985). Stage III chalcopyrite grains contain $\delta^{34}\text{S}$ of -4.6‰ to $+5.2\text{‰}$ (avg. -1.1‰), and $^{206}\text{Pb}/^{204}\text{Pb}$ (18.198–18.987), $^{207}\text{Pb}/^{204}\text{Pb}$ (15.534–15.876), and $^{208}\text{Pb}/^{204}\text{Pb}$ (37.685–39.476).

5. Discussion

5.1. Ore-Forming Material and Fluid Source

Our new carbon–oxygen isotope data clearly show different sources for the Stage II and III fluids. In the $\delta^{13}\text{C}$ vs. $\delta^{18}\text{O}$ diagram (Figure 9), all data fall between the marine carbonate field and the magmatic-related (igneous carbonatite) field, with the Stage II data falling closer to the former and Stage III data falling closer to the latter. This suggests that the Stage II and III fluids were derived mainly from marine carbonates and igneous source, respectively, with different proportions of mixing between the two end-members.

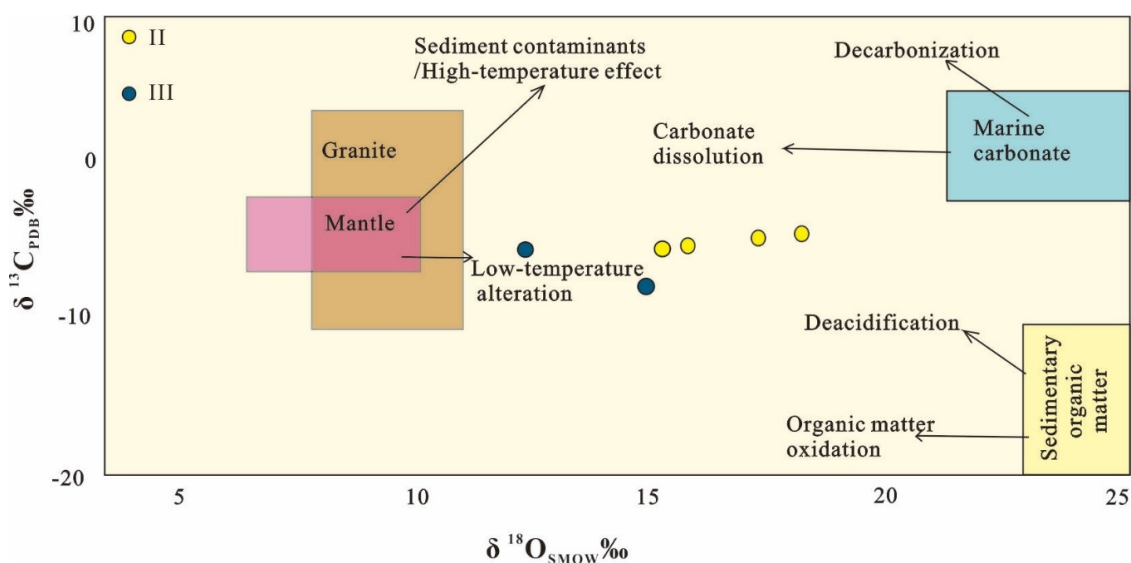


Figure 9. $\delta^{13}\text{C}$ vs. $\delta^{18}\text{O}$ diagram for ore-related calcite from Xianglushan Fe-Cu deposit [33–36].

Sulfur isotopes of Stage III chalcopyrite fall distinctly in a narrower range around zero than those of Stage II pyrite. This demonstrates a likely magmatic source for Stage III chalcopyrite, whilst Stage II

pyrite may have been magmatic-hydrothermal or sedimentary. Although there is a lack of data, the magmatic-source for Stage III ore-forming material is further supported by that $^{207}\text{Pb}/^{204}\text{Pb}$ values for most Stage III chalcopyrite fall between the orogen and mantle evolution curves. Meanwhile, the higher $^{207}\text{Pb}/^{204}\text{Pb}$ values (above the upper crustal evolution curve) for most late Stage II pyrite imply that both magmatic-hydrothermal and sedimentary source are possible for the late Stage II ore-forming material (Figure 10). We propose that ore-forming material in Stage II may have derived from both the wall rocks (carbonates, siliciclastics, and spilite) and local mafic intrusions, whilst in Stage III they may have derived mainly from the intrusions.

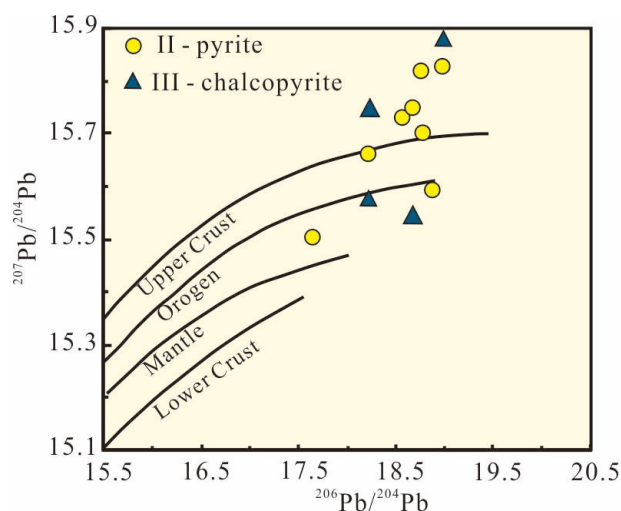


Figure 10. $^{207}\text{Pb}/^{204}\text{Pb}$ vs. $^{206}\text{Pb}/^{204}\text{Pb}$ diagram for ore sulfides from Xianglushan Fe-Cu deposit (modified from Liu et al. [27]).

5.2. Ore Deposit Type and Genesis

Preliminary studies on the Xianglushan Fe-Cu deposits have loosely constrained the deposit type to be magmatic-hydrothermal or (sedimentary exhalative) SEDEX-like. In this study, however, we found that the Fe-(Cu) and Cu mineralization occurred in two different stages, resembling many skarn- or IOCG-type deposits. The Fe mineralization is mainly stratabound and occurs in the upper part of the Yinmin Formation, close to the stratigraphic boundary between the carbonates and spilite. The massive replacement texture of the Fe (magnetite–hematite) ores are also similar to skarn- or IOCG-type mineralization. However, some typical early-stage alteration minerals of skarn (e.g., garnet and pyroxene) and IOCG (e.g., apatite) are not found, although they may be replaced by later alteration and mineralization. The late Stage II disseminated pyrite \pm chalcopyrite mineralization and Stage III vein/stockwork chalcopyrite mineralization has seen an increasing magmatic influence, as supported by C-O-S isotope data. As shown in Figure 11, the $\delta^{34}\text{S}$ values of the Xianglushan ore sulfides (esp. Stage III chalcopyrite) are markedly different from those of typical SEDEX (e.g., Century and Mt Isa, Australia), MVT (e.g., Pine Point, Canada), and Irish-type (e.g., Lischeen, Ireland) deposits, but resemble more those of typical VMS (e.g., Kuroko and Cyprus) and IOCG (e.g., Candelaria) deposits. Besides, the $\delta^{34}\text{S}$ values of the Xianglushan Cu ores are also comparable to those of mafic rocks, which suggest that the Cu mineralization may have been genetically related to the mafic intrusions in the region, although no direct contact relationship is observed ([37–39], ref. contained therein). Although we do not have sulfur isotope data of the sedimentary rocks in the district, it is very likely that the sulfur was derived from a mixture of mafic-rock and sedimentary-related source, as implied by the wide Stage III sulfide $^{207}\text{Pb}/^{204}\text{Pb}$ range and calcite $\delta^{18}\text{O}$ trend.

Similar to many typical IOCG deposits, the Xianglushan mineral system is featured by early Fe and late Cu mineralization, and shows an early sodic-calcic alteration followed by a Fe-ore-related potassic alteration. In Figure 12, it is shown that the ore-forming temperatures of the Xianglushan Stage

II Fe-(Cu) and Stage III Cu mineralization resemble those of the Lala Fe mineralization and the Manto Verde Cu mineralization, respectively. These similarities with typical IOCG deposits, the commonly low Cu-grade and lack of Au, and the submarine volcanic-hosted nature of Xianglushan mimic many IOCG-like mineral systems in the Chinese Eastern Tianshan [40–42], and therefore we suggest that the Xianglushan deposits are also best classified as submarine volcanic-hosted and IOCG-like.

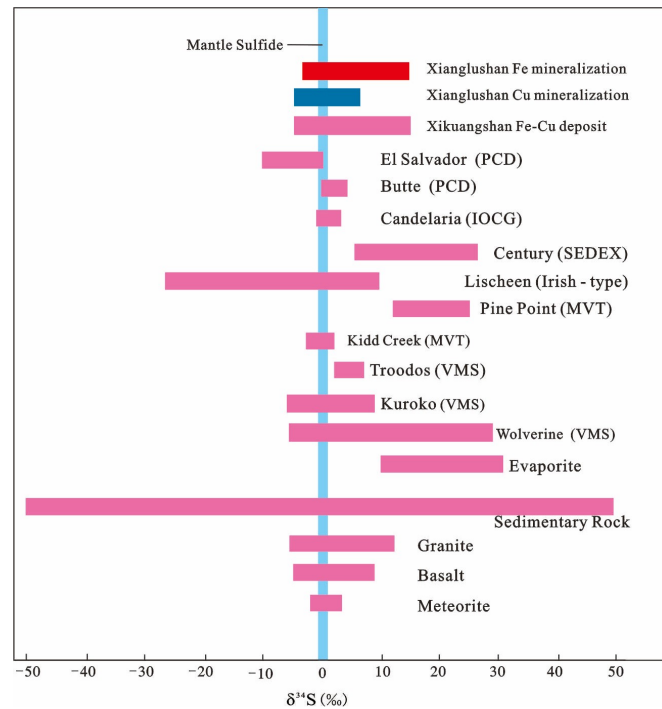


Figure 11. $\delta^{34}\text{S}$ values for sulfides from Xianglushan Stage II pyrite and Stage III chalcopyrite, data from selected base metal deposits, seawater, and rock types around the world, are shown for comparison (e.g., [37–39], and references contained therein).

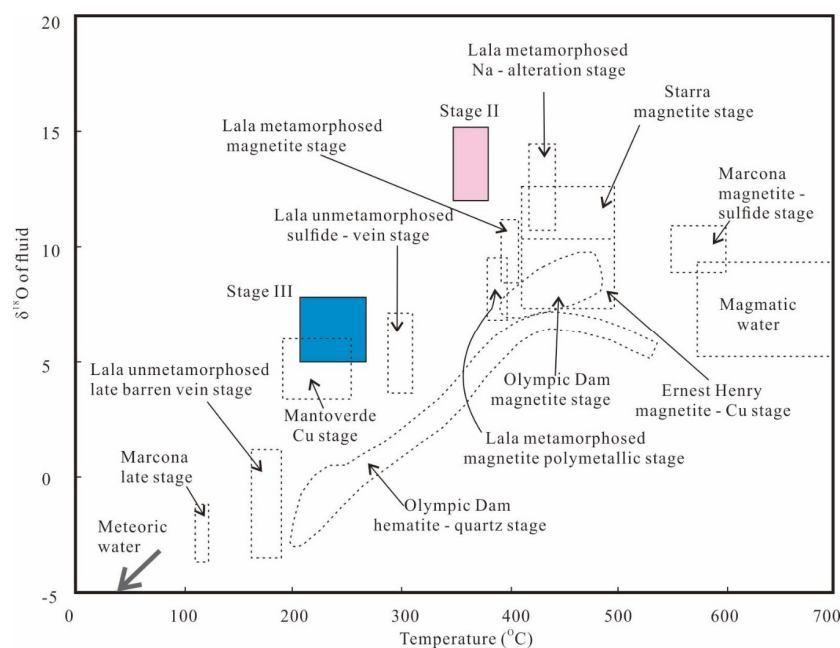


Figure 12. $\delta^{18}\text{O}$ -temperature relationships of the calculated fluids of the Xianglushan Stage II and III fluids and other IOCG deposits in the world. Data for Lala and other IOCG deposits are from Chen and Zhao [43], Chen et al. [44], and Williams et al. [45] (references contained therein).

In recent years, the Lala deposit in the Huili–Dongchuan ore belt has been suggested to be IOCG-type/-like. The Xianglushan Fe–Cu deposits share some similar geological features with the Lala deposit [43], such as being hosted by Paleoproterozoic volcanic-sedimentary rocks, with massive Fe mineralization followed by vein-type Cu mineralization, the lack of apparent magmatic link (albeit some magmatic C–O–Pb–S isotope signatures), and similar range of $\delta^{34}\text{S}$ values. However, the Xianglushan Fe–Cu mineralization is different from its Lala counterpart in its lower content (or absence) of gold, apatite, and molybdenite, and the lack of breccia ores. More detailed fluid inclusion and geochronological work is needed to decipher if the Xianglushan Fe–Cu deposits are part of the “Kangdian IOCG metallogenic province” proposed by Zhao and Zhou [10].

With the new geology, fluid inclusion, and C–O–S–Pb isotope data, we propose a new two-stage metallogenic model for the IOCG-like Xianglushan Fe–Cu deposits (Figure 13). During the Mesoproterozoic (~1100 Ma) or Neoproterozoic [10], gradual closure of the Anning Ocean may have generated an intra-/back-arc basin now situated along the Huili–Dongchuan ore belt. The intra-/back-arc rifting may have led to extensive basaltic volcanism (now spilite and tuff of the Yinmin Formation) and carbonate deposition (Dongchuan Group). The subsequent back-arc basin inversion may have heated up and driven the oxidized seawater to react with the mafic wall rocks, forming the Stage II magnetite–hematite mineralization and the associated alterations. Continuous fluid–wall rock reactions and Fe-oxide precipitation with possible magmatism may have created a more reduced, Fe-poor fluid with a stronger magmatic signature, which may have led to the subsequent Stage III chalcopyrite mineralization. Post-mineralization thick calcite veining followed when the hydrothermal fluids were depleted of copper (and other metals) and sulfur.

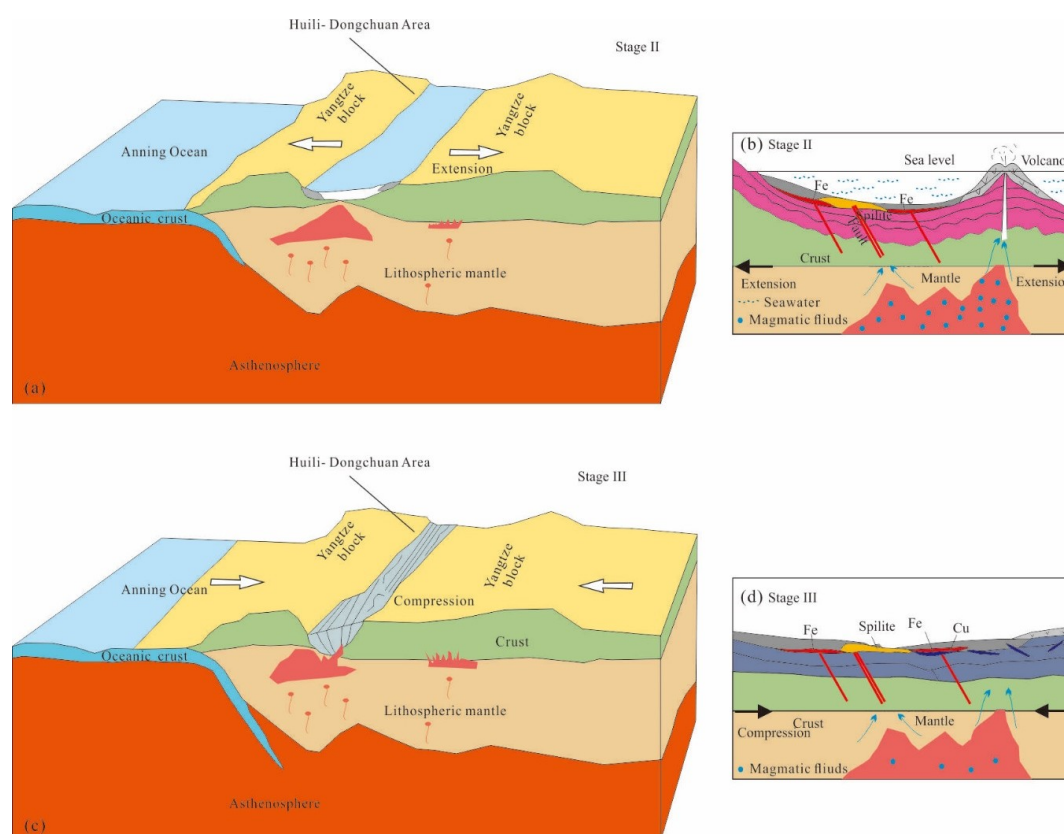


Figure 13. Schematic ore deposit model for the two-stage mineralization in the Xianglushan Fe–Cu orefield; (a) Tectonic setting of Huili–Dongchuan at Stage II, showing the formation of a backarc basin; (b) Stage II mineralization, showing the formation of Fe orebodies; (c) Tectonic setting of Huili–Dongchuan at Stage III, showing the backarc basin inversion; (d) Stage III mineralization, showing the formation of Cu orebodies.

6. Conclusions

Our new geology, fluid inclusion, and C-O-S-Pb isotope data suggest that the Xianglushan Fe-Cu ore formation was a two-stage process. The earlier stratiform Fe oxide ore formation was produced by a medium-high temperature, oxidized Fe-rich ore fluid of mixed meteoric (e.g., seawater)-magmatic origin (mainly meteoric), whilst the later vein-type chalcopyrite ore formation was produced by a medium-temperature, reduced Fe-poor ore fluid of mixed magmatic-meteoric origin (mainly magmatic). The two-stage mineralization process, the alteration styles (sodic-calcic followed by ore-related potassic), the ore fluid temperatures, and the isotope characters of the Xianglushan Fe-Cu mineralization resemble many IOCG-type deposits, yet the Cu-Au poor nature and the lack of apatite are atypical of the IOCG-style. Therefore, we propose that the Xianglushan Fe-Cu mineralization is submarine volcanic-sedimentary rock-hosted and IOCG-like, and was formed probably in an intra-/back-arc basin inversion setting related to the closure of the Mesoproterozoic Anning Ocean.

Author Contributions: Conceptualization, T.W. and C.L.; methodology, H.L.; software, T.W.; validation, T.W. and H.L.; formal analysis, T.W.; investigation, T.W.; resources, T.W.; data curation, H.L.; writing—original draft preparation, T.W. and C.L.; writing—review and editing, C.L.; visualization, T.W. and H.L.; supervision, T.W.; project administration, T.W.; funding acquisition, T.W.

Funding: This research was funded by the National Natural Science Foundation of China (Grant No. 41502067).

Acknowledgments: We thank the staff from the Xianglushan Fe-Cu mines for helping with the field work. The Editor and Guest Editor Fernando Henriquez and two anonymous reviewers are thanked for their insightful comments, which significantly enhanced the manuscript.

Conflicts of Interest: The authors declare no conflict of interest.

References

1. Zhao, X.F.; Zhou, M.F.; Li, J.W.; Sun, M.; Gao, J.F.; Sun, W.H.; Yang, J.H. Late Paleoproterozoic to early Mesoproterozoic Dongchuan Group in Yunnan, SW China: Implications for tectonic evolution of the Yangtze Block. *Precambrian Res.* **2010**, *182*, 57–69. [[CrossRef](#)]
2. Peng, M.; Wu, Y.B.; Gao, S.; Zhang, H.F.; Wang, J.; Liu, X.C.; Gong, H.J.; Zhou, L.; Hu, Z.C.; Liu, Y.S.; et al. Geochemistry, Zircon U-Pb Age and Hf Isotope Compositions of Paleoproterozoic Aluminous A-type Granites from the Kongling Terrain, Yangtze Block: Constraints on Petrogenesis and Geologic Implications. *Gondwana Res.* **2012**, *22*, 140–151. [[CrossRef](#)]
3. Zhang, D.L.; Huang, D.Z.; Zhang, H.F.; Wang, G.Q.; Du, G.F. Chronological framework of basement beneath the Xianmgzhong Basin: Evidence by U-Pb ages of detrital zircons from Xikuangshan. *Acta Petrol. Sin.* **2016**, *32*, 3456–3468. (In Chinese)
4. Greentree, M.R.; Li, Z. The oldest known rocks in south western China: SHRIMP U-Pb magmatic crystallization age and detrital provenance analysis of the Paleoproterozoic Dahongshan Group. *J. Asian Earth Sci.* **2008**, *33*, 289–302. [[CrossRef](#)]
5. Sun, W.H.; Zhou, M.F.; Gao, J.F.; Yang, Y.H.; Zhao, X.F.; Zhao, J.H. Detrital zircon U-Pb geochronological and Lu-Hf isotopic constraints on the Precambrian magmatic and crustal evolution of the western Yangtze Block, SW China. *Precambrian Res.* **2009**, *172*, 99–126. [[CrossRef](#)]
6. Greentree, M.R.; Li, Z.X.; Li, X.H.; Wu, H. Late Mesoproterozoic to earliest Neoproterozoic basin record of the Sibao Orogenesis in western South China and relationship to the assembly of Rodinia. *Precambrian Res.* **2006**, *151*, 79–100. [[CrossRef](#)]
7. Fan, H.P.; Zhu, W.G.; Li, Z.X.; Zhong, H.; Bai, Z.J.; He, D.F.; Chen, C.J.; Cao, C.Y. Ca. 1.5 Ga mafic magmatism in South China during the break-up of the supercontinent Nuna/Columbia: The Zhuqing Fe-Ti-V oxide ore-bearing mafic intrusions in western Yangtze Block. *Lithos* **2013**, *16*, 85–98. [[CrossRef](#)]
8. Chen, W.T.; Zhou, M.F.; Gao, J.F.; Hu, R.Z. Geochemistry of magnetite from Proterozoic Fe-Cu deposits in the Kangdian metallogenic province, SW China. *Miner. Depos.* **2015**, *50*, 795–809. [[CrossRef](#)]
9. Zeng, M.; Zhang, D.; Zhang, Z.; Li, T.; Li, C.; Wei, C. Structural controls on the Lala Iron-Copper Deposit of the Kangdian metallogenic province, southwestern China: Tectonic and metallogenic implications. *Ore Geol. Rev.* **2018**, *97*, 35–54. [[CrossRef](#)]

10. Zhao, X.F.; Zhou, M.F. Fe–Cu deposits in the Kangdian region, SW China: a Proterozoic IOCG (iron-oxide–copper–gold) metallogenic province. *Miner. Depos.* **2011**, *46*, 731–747. [[CrossRef](#)]
11. Gong, L. The metallogenetic rule and prospecting of middle Proterozoic Cu–Fe metallogenetic zone in central Yunnan. *Yunnan Geol.* **2011**, *30*, 255–260. (In Chinese)
12. Liu, W.; Yang, X.; Shu, S.; Liu, L.; Yuan, S. Precambrian Basement and Late Paleoproterozoic to Mesoproterozoic Tectonic Evolution of the SW Yangtze Block, South China: Constraints from Zircon U–Pb Dating and Hf Isotopes. *Minerals* **2018**, *8*, 333. [[CrossRef](#)]
13. Wang, D.B.; Yin, F.G.; Sun, Z.M.; Wang, L.Q.; Wang, B.D.; Liao, S.Y.; Tang, Y.; Ren, G.M. Zircon U–Pb age and Hf isotope of Paleoproterozoic mafic intrusion on the western margin of the Yangtze Block and their implications. *Geol. Bull. China* **2013**, *32*, 617–630. (In Chinese)
14. Zhu, H.; Fan, H.; Fan, W.; Zhou, B.; Wang, S.; Luo, M.; Liao, Z.; Guo, Y. Assessing Precambrian stratigraphic sequence of Dongchuan area: Evidence from zircon SHRIMP and LA-ICP-MS dating. *Geol. J. Chin. Univ.* **2011**, *17*, 452–461. (In Chinese)
15. Zhou, B.; Wang, S.; Sun, X.; Liao, Z.; Guo, Y.; Jiang, X.; Zhu, H.; Liu, M.; Ma, D.; Shen, Z.; et al. SHRIMP U–Pb age and its significance of zircons in welded tuff of Wangchang formation in Dongchuan area, Yunnan province, SW China. *Geol. Rev.* **2012**, *58*, 359–368. (In Chinese)
16. Hu, Z.C.; Liu, Y.S.; Gao, S.; Liu, W.G.; Zhang, W.; Tong, X.R.; Lin, L.; Zong, K.Q.; Li, M.; Chen, H.H.; et al. Improved in situ Hf isotope ratio analysis of zircon using newly designed X skimmer cone and Jet sample cone in combination with the addition of nitrogen by laser ablation multiple collector ICPMS. *J. Anal. Atom. Spectrom.* **2012**, *27*, 1391–1399. [[CrossRef](#)]
17. Wang, L.J.; Griffin, W.L.; Yu, J.H.; O’Reilly, S.Y. U–Pb and Lu–Hf Isotopes in Detrital Zircon from Neoproterozoic Sedimentary Rocks in the Northern Yangtze Block: Implications for Precambrian Crustal Evolution. *Precambrian Res.* **2013**, *23*, 1261–1272. [[CrossRef](#)]
18. Wang, W.; Zhou, M.F. Provenance and tectonic setting of the Paleo–Mesoproterozoic Dongchuan Group in the southwestern Yangtze Block, South China: Implication for the breakup of the supercontinent Columbia. *Tectonophysics* **2014**, *610*, 110–127. [[CrossRef](#)]
19. Yang, H.; Liu, P.H.; Meng, E.; Wang, F.; Xiao, L.L.; Liu, C.H. Geochemistry and its tectonic implications of metabasite in the Dahongshan Group in southwestern Yangtze block. *Acta Petrol. Sin.* **2014**, *30*, 3021–3033. (In Chinese)
20. Gong, L.; He, Y.; Chen, T.; Zhao, Y. *Proterozoic Rift Type Copper Deposit in Dongchuan, Yunnan*; Wang, X., Ed.; Metallurgical Industry Press: Beijing, China, 1996; pp. 6–50. (In Chinese)
21. Wang, S.; Liao, Z.; Sun, X.; Zhou, Q.; Wang, B.; Wang, Z.; Guo, Y.; Jiang, X.; Yang, B.; Lu, S. The Yanshanian Lithospheric Evolution in Kangdian Area—Restriction from SHRIMP Zircons U–Pb Age and Geochemistry of Mafic Dykes in Dongchuan, Yunnan Province, SW China. *Acta Petrol. Sin.* **2014**, *88*, 299–317. (In Chinese)
22. Brown, P.E.; Lamb, W.M. P–V–T properties of fluids in the system $\text{H}_2\text{O} \pm \text{CO}_2 \pm \text{NaCl}$: New graphical presentations and implications for fluid inclusion studies. *Geochim. Cosmochim. Acta* **1989**, *53*, 1209–1221. [[CrossRef](#)]
23. Wang, L.J. Analysis and study of the composition of fluid inclusions. *Geol. Rev.* **1998**, *44*, 496–501. (In Chinese)
24. Zhu, H.P.; Wang, L.J.; Liu, J.M. Determination of quadruple mass spectrometer for gaseous composition of fluid inclusion from different mineralization stages. *Acta Petrol. Sin.* **2003**, *19*, 314–318. (In Chinese)
25. Guo, L.; Hou, L.; Liu, S.; Nie, F. Rare Earth Elements Geochemistry and C–O Isotope Characteristics of Hydrothermal Calcites: Implications for Fluid–Rock Reaction and Ore–Forming Processes in the Phapon Gold Deposit, NW Laos. *Minerals* **2018**, *8*, 438. [[CrossRef](#)]
26. Yuan, S.; Peng, J.; Li, X.; Peng, Q. Carbon, Oxygen and Strontium Isotope geochemistry of calcites from the Xianghualing Tin–Polymetallic Deposit, Hunan Province. *Acta Geol. Sin.* **2008**, *82*, 1522–1530. (In Chinese)
27. Liu, Q.; Shao, Y.; Liu, Z.; Zhang, J.; Wang, C. Origin of the Granite Porphyry and Related Xiajinbao Au Deposit at Pingquan, Hebei Province, Northeastern China: Constraints from Geochronology, Geochemistry, and H–O–S–Pb–Hf Isotopes. *Minerals* **2018**, *8*, 330. [[CrossRef](#)]
28. Wu, J.H.; Li, H.; Algeo, T.J.; Jiang, W.C.; Zhou, Z.K. Genesis of the Xianghualing Sn–Pb–Zn deposit, South China: A multi-method zircon study. *Ore Geol. Rev.* **2018**, *102*, 220–239. [[CrossRef](#)]
29. Li, H.; Wu, Q.H.; Evans, N.J.; Zhou, Z.K.; Kong, H.; Xi, X.S.; Lin, Z.W. Geochemistry and geochronology of the Banxi Sb deposit: Implications for fluid origin and the evolution of Sb mineralization in central-western Hunan, South China. *Gondwana Res.* **2018**, *55*, 112–134. [[CrossRef](#)]

30. Todt, W.; Cliff, R.A.; Hanser, A.; Hofmann, A.W. Evaluation of a ^{202}Pb - ^{205}Pb double spike for high-precision lead isotope analysis. *Geophys. Monograph Ser.* **1996**, *95*, 429–437.
31. Lu, H.Z.; Fan, H.R.; Ni, P.; Ou, X.; Shen, K.; Zhang, W. *Fluid Inclusions*; Hu, X., Hu, S., Eds.; Science Press: Beijing, China, 2004; pp. 1–48.
32. O’Neil, J.R.; Clayton, R.N.; Mayade, T.K. Oxygen isotope fractionation in divalent metal carbonates. *J. Chem. Phys.* **1969**, *51*, 5547–5558. [[CrossRef](#)]
33. Sun, J.G.; Hu, S.X.; Shen, K. Research on C, O isotopic geochemistry of intermediate-basic and intermediate-acid dykes in gold fields of Jiaodong Peninsular. *Acta Petrol. Mineral.* **2001**, *20*, 46–56. (In Chinese)
34. Deines, P. Stable isotope variations in carbonatites. In *Carbonatites: Genesis and Evolution*; Bell, K., Ed.; Springer: Berlin/Heidelberg, Germany, 1989; pp. 301–359.
35. Taylor, H.P.; Frechen, J.; Degens, E.T. Oxygen and carbon isotope studies of carbonatites from the Laacher See District, West Germany and the Alnö District, Sweden. *Geochim. Cosmochim. Acta* **1967**, *31*, 407–431. [[CrossRef](#)]
36. Demény, A.; Ahijado, A.; Casillas, R.; Vennemann, T.W. Crustal contamination and fluid/rock interaction in the carbonatites of Fuerteventura (Canary Islands, Spain): A C, O, H isotope study. *Lithos* **1998**, *44*, 101–115. [[CrossRef](#)]
37. Hoefs, J. *Stable Isotope Geochemistry*; Springer Science & Business Media: Berlin/Heidelberg, Germany, 2008.
38. Li, R.; Chen, H.; Xia, X.; Yang, Q.; Danyushevsky, L.V.; Lai, C.K. Using integrated in-situ sulfide trace element geochemistry and sulfur isotopes to trace ore-forming fluids: Example from the Mina Justa IOCG deposit (southern Perú). *Ore Geol. Rev.* **2018**, *101*, 165–179. [[CrossRef](#)]
39. Monteiro, L.; Xavier, R.; Carvalho, E.; Hitzman, W.; Johnson, C.; Souza, F.; Torresi, I. Spatial and temporal zoning of hydrothermal alteration and mineralization in the Sossego iron oxide-copper-gold deposit, Carajás Mineral Province, Brazil: Paragenesis and stable isotope constraints. *Miner. Depos.* **2008**, *43*, 129–159. [[CrossRef](#)]
40. Han, J.; Chen, H.; Jiang, H.; Zhao, L.; Zhang, W.; Lai, C.K. Genesis of the Paleozoic Aqishan-Yamansu arc-basin system and Fe (-Cu) mineralization in the Eastern Tianshan, NW China. *Ore Geol. Rev.* **2019**, *105*, 55–70. [[CrossRef](#)]
41. Liang, P.; Chen, H.; Han, J.; Wu, C.; Zhang, W.; Xu, D.; Lai, C.K.; Kyser, K. Iron oxide-copper-gold mineralization of the Devonian Laoshankou deposit (Xinjiang, NW China) in the Central Asian Orogenic Belt. *Ore Geol. Rev.* **2019**, *104*, 628–655. [[CrossRef](#)]
42. Zhang, W.; Chen, H.; Peng, L.; Zhao, L.; Huang, J.; Lu, W.; Liang, P.; Lai, C. Discriminating hydrothermal fluid sources using tourmaline boron isotopes: Example from Bailingshan Fe deposit in the Eastern Tianshan, NW China. *Ore Geol. Rev.* **2018**, *98*, 28–37. [[CrossRef](#)]
43. Chen, W.T.; Zhou, M.F. Paragenesis, Stable Isotopes, and Molybdenite Re-Os Isotope Age of the Lala Iron-Copper Deposit, Southwest China. *Econ. Geol.* **2012**, *107*, 459–480. [[CrossRef](#)]
44. Chen, H.; Kyser, T.K.; Clark, A.H. Contrasting fluids and reservoirs in the contiguous Marcona and Mina Justa iron oxide-Cu (-Ag-Au) deposits, south-central Peru. *Miner. Depos.* **2011**, *46*, 677–706. [[CrossRef](#)]
45. Williams, P.J.; Barton, M.D.; Johnson, D.A.; Fontbote, L.; De Haller, A.; Mark, G.; Oliver, N.H.S.; Marschik, R. Iron oxide copper-gold deposits: Geology, space-time distribution, and possible modes of origin. *Econ. Geol.* **2005**, *100*, 371–405.

